



Properties of Electron-scale Magnetic Reconnection at a Quasi-perpendicular Shock

Ao Guo^{1,2,3} , Quanming Lu^{1,2,3} , San Lu^{1,2,3} , Shimou Wang^{1,2,3} , and Rongsheng Wang^{1,2,3} ¹ Deep Space Exploration Laboratory, School of Earth and Space Sciences, University of Science and Technology of China, Hefei 230026, People's Republic of China; qmlu@ustc.edu.cn² CAS Center for Excellence in Comparative Planetology, CAS Key Lab of Geospace Environment, Hefei 230026, People's Republic of China; lusan@ustc.edu.cn³ Collaborative Innovation Center of Astronautical Science and Technology, Harbin, People's Republic of China

Received 2023 June 6; revised 2023 July 27; accepted 2023 July 30; published 2023 September 12

Abstract

Recent spacecraft observations have shown that magnetic reconnection occurs commonly in turbulent environments at shocks. At quasi-perpendicular shocks, magnetic field lines are bent by the back-streaming reflected ions, which form a current sheet in the foot region, and then electron-scale reconnection occurs when the current sheet is fragmented at the shock front. Here we study magnetic reconnection at a quasi-perpendicular shock by using a two-dimensional particle-in-cell simulation. Collective properties of the reconnection sites from the shock transition to the downstream region are analyzed by adopting a statistical approach to the simulation data. Reconnecting current sheets are found to be densely distributed near the shock front, with a reconnection electric field larger than those in the downstream region. By tracing a reconnection site from its formation until it is convected downstream, we show the reconnection proceeds intermittently after an active stage near the shock front. Our tracing further shows that, in addition to being originated from the shock front, reconnection in the downstream region can also occur locally, driven by turbulent flows therein. The results help us better understand the evolution of electron-scale reconnection at a perpendicular shock.

Unified Astronomy Thesaurus concepts: [Space plasmas \(1544\)](#); [Plasma physics \(2089\)](#); [Solar magnetic reconnection \(1504\)](#); [Planetary bow shocks \(1246\)](#)

Supporting material: animations

1. Introduction

Collisionless shock waves are important nonlinear phenomena commonly observed in the space plasma environment, such as the Earth's bow shock and interplanetary shocks (Sagdeev 1966; Russell et al. 1982; Tsurutani & Stone 1985; Bavassano-Cattaneo et al. 1986; Turner et al. 2018; Yang et al. 2020). The structure and dynamics of the shock are affected by the angle between the upstream magnetic field and the shock normal θ_{Bn} . They are then classified as quasi-perpendicular shocks with $\theta_{Bn} > 45^\circ$ and quasi-parallel shocks with $\theta_{Bn} < 45^\circ$ (Bale et al. 2005; Burgess et al. 2005; Balogh & Treumann 2013). Both the quasi-perpendicular and quasi-parallel shocks have a shock transition region where the plasma properties change abruptly from the upstream to the downstream. Various instabilities and waves are generated in the transition and downstream region, creating a turbulent environment filled with small-scale fluctuations in the magnetic field and the plasma characteristics (McKean et al. 1992; Matsukiyo & Scholer 2003; Lu & Wang 2005; Matsukiyo & Scholer 2006; Hao et al. 2014; Dimmock et al. 2019; Gingell et al. 2020).

By creating regions of antiparallel magnetic fields, turbulence can trigger magnetic reconnection, which changes the magnetic topology and transfers the energy from electromagnetic fields to particles (Lazarian & Vishniac 1999; Servidio et al. 2010; Comisso & Sironi 2018; Lazarian et al. 2020; Comisso & Sironi 2022; Li et al. 2022). In situ evidences of magnetic reconnection in the shock transition region and the

downstream magnetosheath have been provided by Cluster and Magnetospheric Multiscale (MMS) satellite observations (Retinò et al. 2007; Yordanova et al. 2016; Vörös et al. 2017; Gingell et al. 2019; Phan et al. 2018; Wang et al. 2019; Stawarz et al. 2019; Wang et al. 2021; Zhong et al. 2022). Reconnection may play a role in dissipating turbulence and repartitioning energy in this region.

At quasi-parallel shocks, a portion of upstream ions is reflected by the shock and streams back along the magnetic field lines, exciting ultralow frequency (ULF) waves through the ion–ion beam instability in the upstream region (Scholer 1990; Le & Russell 1992; Su et al. 2012; Wu et al. 2015; Hao et al. 2016). These waves perturb the magnetic field lines and cause magnetic reconnection between them in the downstream magnetosheath (Lu et al. 2020a). In addition, waves with shorter wavelengths are also found to be excited in the transition region, generating reconnection sites in electron-scale current sheets (Bessho et al. 2020). Magnetic reconnection typically forms electron and ion bidirectional outflows. Sometimes, reconnection in turbulent environments at quasi-parallel shocks forms only the electron outflows without any ion outflows, and therefore, such a type of reconnection is referred to as “electron-only” reconnection (Phan et al. 2018; Wang et al. 2018; Pyakurel et al. 2019; Lu et al. 2020b, 2022). Moreover, a tendency that the reconnection electric field increases with the electron outflow speed has been found in a two-dimensional (2D) particle-in-cell (PIC) simulation of the quasi-parallel shock (Bessho et al. 2022).

Due to the lack of interaction of reflected particles and waves in the upstream region, the transition region of quasi-perpendicular shocks is usually less extended and less turbulent than that of quasi-parallel shocks (Gurnett et al. 1979; Burgess et al. 2005; Bale et al. 2005; Dimmock et al. 2019; Gingell

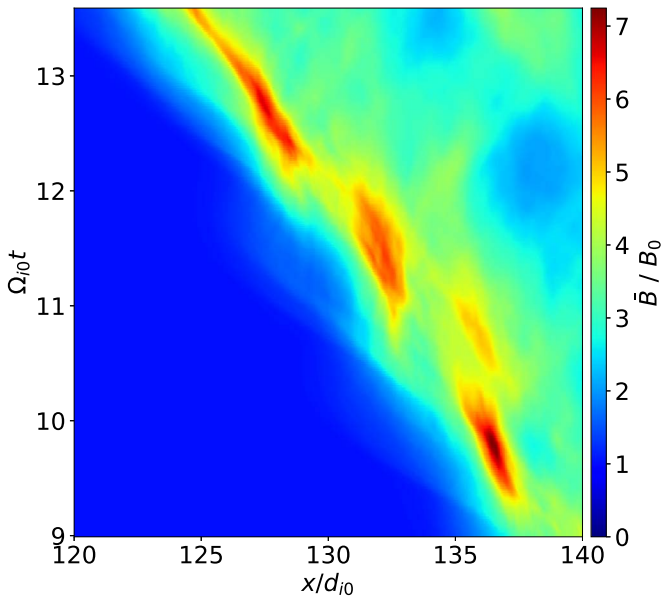


Figure 1. Temporal evolution of the magnetic field strength \bar{B} from $\Omega_{i0}t = 9$ –13.61. Here, \bar{B} is the magnetic field strength $\bar{B} = \sqrt{B_x^2 + B_y^2 + B_z^2}$ averaged over y -direction.

et al. 2020). As a result, reconnection seems unlikely to take place at quasi-perpendicular shocks. However, a statistical survey of Earth’s bow shock demonstrated that reconnection at quasi-perpendicular shocks also occurs frequently (Gingell et al. 2020). By using PIC simulations, Lu et al. (2021) showed the occurrence of magnetic reconnection at the quasi-perpendicular shocks and found that a current sheet is produced by the back-streaming reflected ions in the foot region of the quasi-perpendicular shock, and electron-scale reconnection occurs in this current sheet when it is convected to the shock front by the solar wind.

Magnetic reconnection in the turbulent transition region of quasi-perpendicular shock provides us with a new scenario of kinetic scale reconnection. However, much of its nature remains unclear. For example, how does the reconnection site evolve from its formation to being convected downstream? What are the properties of reconnection sites at different locations of the shock? To answer these questions, we analyze the relationship between magnetic reconnection and shock by adopting a statistical approach to the simulation data. A challenging problem we must solve first is how to identify the reconnection events in the turbulent shock transition region. The plasma outflow jet is often used as an important criterion for the identification of reconnection events in observations (Gingell et al. 2020). However, simulations have shown that the structure of reconnection regions in shock turbulence has asymmetric inflows and outflows (Bessho et al. 2019, 2020), which is different from laminar reconnection regions and can cause an underestimation of reconnection sites in observations. In PIC simulations of the shock, an efficient way to identify all the reconnection sites except for manual selection is still lacking. This problem is solved in this paper by using a combination method of saddle-point identification and clustering algorithm. In this way, the statistics of physical quantities such as the reconnection electric field at all the saddle points can be obtained. We also trace individual reconnection sites to explore their evolution and examine the magnetic flux transport at these points to determine whether they are actively

reconnecting. The simulation model is described in Section 2, the simulation results are presented in Section 3, and Section 4 is the conclusions and discussion.

2. Simulation Setup

An open-source relativistic full PIC code named SMILEI (Derouillat et al. 2018) is employed. Particles have two spatial and three velocity components (2D3V) in our simulation. The shock wave is generated by the injection method, in which particles are continuously injected from the left boundary ($x = 0$) at a super-Alfvénic speed V_{in} and then reflected specularly at the right boundary ($x = L_x$). Here we adopt $V_{in} = 7V_{A0}$, where V_{A0} is the Alfvén speed evaluated using the upstream plasma density n_0 and magnetic field B_0 . As a result, a shock is formed and propagates toward the $-x$ -direction when the reflected particles interact with the upstream flow. The simulation is performed in the x – y plane, while periodic boundary condition is applied in the y -direction. The ambient magnetic field is set to have a strong out-of-plane component: $\mathbf{B}_0 = B_0(\cos\theta_{Bn}\mathbf{e}_x + \sin\theta_{Bn}\mathbf{e}_z)\mathbf{e}$ $\theta_{Bn} = 75^\circ$, meaning that a quasi-perpendicular shock is produced.

The mass ratio between ion and electron is reduced to $\frac{m_i}{m_e} = 64$, and the light speed is $c = 28V_{A0}$. The size of the simulation domain is $L_x \times L_y = 163.84d_{i0} \times 12d_{i0}$ (where $d_{i0} = \sqrt{\frac{m_i}{\mu_0 n_0 e^2}}$ is the ion inertial length in the upstream region). Each cell has the size of $\Delta x = \Delta z = 0.01d_{i0}$ and contains 100 ions and electrons initially. The ion and electron beta values in the upstream region are $\beta_{i0} = 0.1$ and $\beta_{e0} = 0.2$.

3. Results

The evolution of the magnetic field \bar{B} from $\Omega_{i0}t = 9$ to 13.61 is shown in Figure 1 (where B is the magnetic field strength $B = \sqrt{B_x^2 + B_y^2 + B_z^2}$ averaged over the y -direction). There is a considerable distance between the shock and the right boundary of the simulation domain during this period, making the boundary effects negligible. The shock wave propagates in the $-x$ -direction at a speed of about $3.05V_{A0}$; the Alfvén Mach number of the shock is thus about 10. The magnetic field of the shock evolves quasi-periodically because of the shock-reformation process (Biskamp & Welter 1972; Lembège & Dawson 1987; Lembège & Savoini 2002; Lobzin et al. 2007; Yang et al. 2009, 2020). There are three cycles of shock reformation in the presented time period.

The 2D structure of the shock at $\Omega_{i0}t = 13.01$ is shown in Figure 2, in which many magnetic islands formed in the distorted current sheets can be observed in the shock ramp and the downstream region (an animation of their formation is available). The formation mechanism of these coherent structures has been revealed in previous work (Lu et al. 2021): The shock-reflected gyrating ions bend the upstream magnetic field lines, resulting in the formation of a current sheet in the foot region ($x < 126d_{i0}$). This process is similar to the instability described in Burgess & Scholer (2007), which exhibits 2D hybrid simulation of perpendicular shock by applying a magnetic field geometry perpendicular to the simulation plane. The mechanism behind this instability involves a modulation of the reflected ion fraction, leading to higher ion-reflection rates at certain locations at the shock and lower or zero reflection at others. It has been demonstrated that this instability can generate current sheets with a width on the order of a few d_{i0} . This electron-scale current sheet then

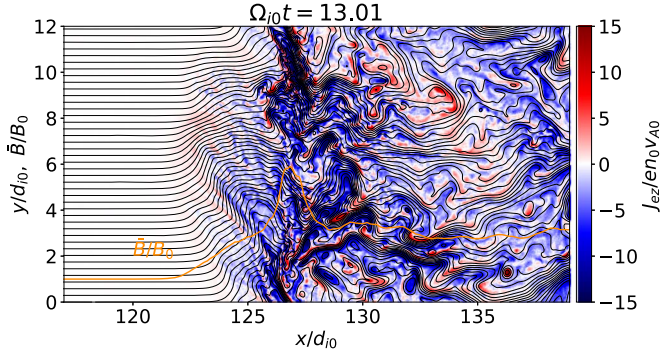


Figure 2. In-plane magnetic field lines and the out-of-plane electron current J_{ez} at $\Omega_{i0}t = 13.01$. The averaged magnetic field \bar{B} is also plotted by the orange line, indicating the shock front is located at about $x = 127d_{i0}$. It shows the time evolution of the shock structure from $\Omega_{i0}t = 12.63$ to 13.35.

(An animation of this figure is available.)

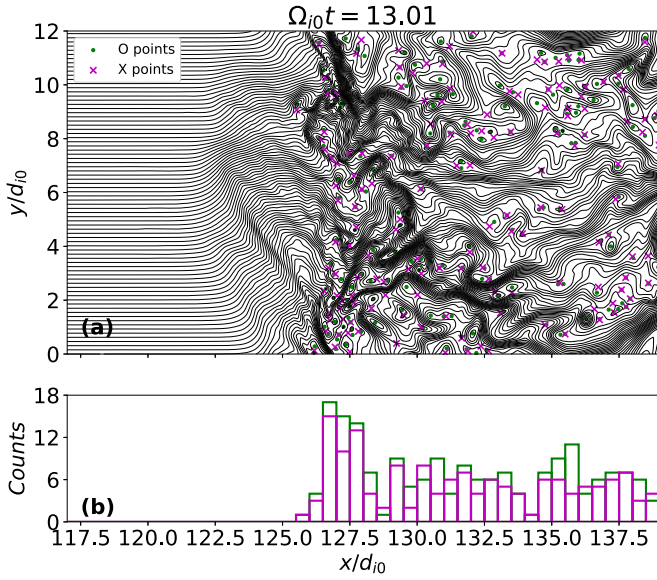


Figure 3. Spatial distribution of identified X points and O points. (a) Identified X (magenta “x”) and O (green dot) points marked on the in-plane magnetic field line (black line). (b) Histogram of X (magenta) and O (green) point distribution on the x -axis.

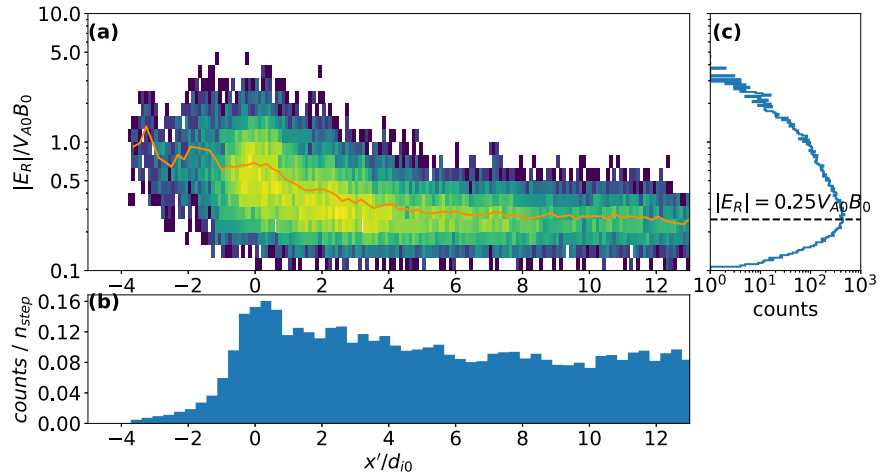


Figure 4. Distribution of the reconnection electric field at X points from $\Omega_{i0}t = 9$ –13.61. (a) Distribution of the X points in the $|E_R| - x'$ space. The orange line plots the $|E_R|$ averaged on the X points located near a given x' . (b) Count rates of the X points on x -axis in the shock rest frame, which is the total number of X points that appeared at x' divided by the number of time steps (n_{step}) when the location x' is included in the diagnostic domain ($x = 120$ – $140d_{i0}$). (c) Distribution of the reconnection electric field $|E_R|$.

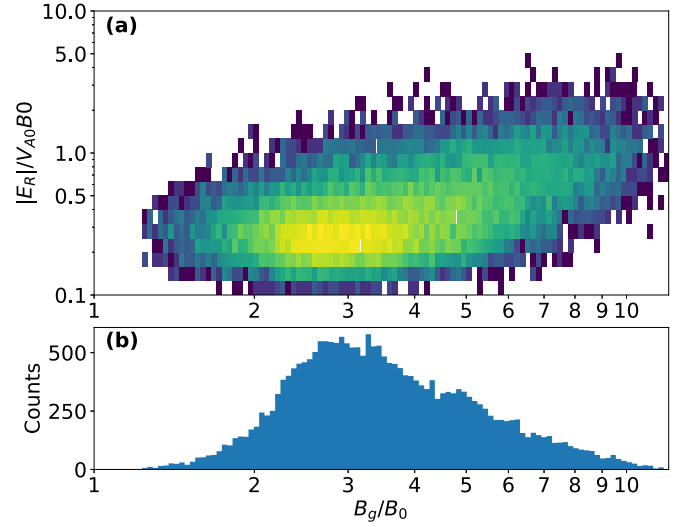


Figure 5. Distribution and correlation between the reconnection electric field and the guide field at X points from $\Omega_{i0}t = 9$ –13.61. (a) Distribution of the X points in the $|E_R| - B_g$ space. (b) Distribution of the guide field B_g at X points.

interacts with the shock front, which can result in magnetic reconnection in the shock transition region. Here we focus on the properties of such a type of reconnection, especially the spatial distribution of the reconnection sites and the reconnection electric field.

3.1. Statistical Properties of Reconnection

To explore the statistical characteristics of magnetic reconnection in the shock transition region, we first identify the exact location of every reconnection site. Here, we employ a method commonly used for saddle-point identification in 2D turbulent plasma (Servidio et al. 2009; Haggerty et al. 2017). First, grid points with zero in-plane magnetic field components ($B_p = 0$) are identified as null points. The Hessian matrices $H_{i,j} = \frac{\partial^2 a}{\partial x \partial y}$ (where a is the magnetic vector potential of the in-plane field defined by $B_p = \nabla a \times \mathbf{e}_z$) and their eigenvalues at these null points are then calculated. If the two eigenvalues share the same sign ($\lambda_1 \lambda_2 > 0$), the null point has a

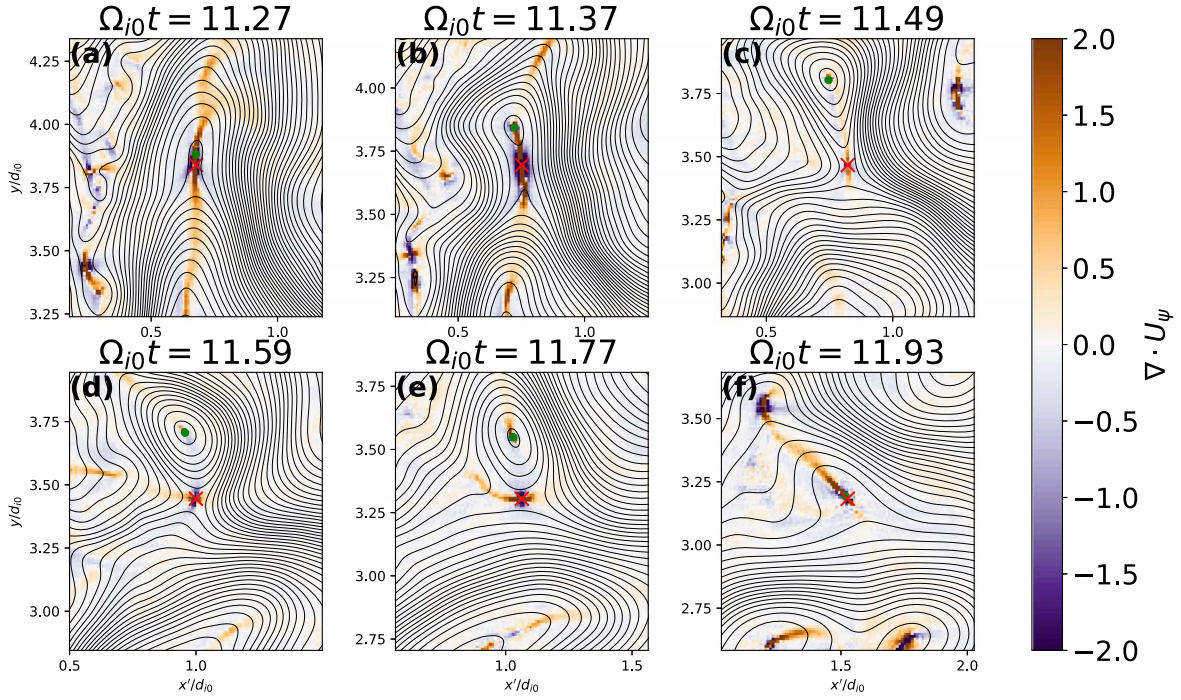


Figure 6. Divergence of the magnetic flux transport $\nabla \cdot U_\psi$, at a traced X point at $\Omega_{i0}t = 11.27, 11.37, 11.49, 11.59, 11.77,$ and 11.93 . The black lines represent the in-plane magnetic field line. The X and O points we traced are marked by the red “X” and green dot. An animation of this figure shows the evolution of the traced X and O points from $\Omega_{i0}t = 11.27$ – 11.93 .

(An animation of this figure is available.)

maximum or minimum magnetic vector potential. We call these kinds of points “O points” because they are always located at the center of magnetic islands. On the other hand, those null points whose eigenvalues have a different sign ($\lambda_1 \lambda_2 < 0$) are named “X points.” Note that an X point we define here is just a saddle point in magnetic topology, which may not be an active reconnection site. Due to the finite differences in space and the limited number of macro-particles per cell, the magnetic field in PIC simulation has particle noise at scales under the Debye length, which can lead to a large overestimation of the null points. To avoid this numerical issue, we use a clustering algorithm called density-based spatial clustering of applications with noise (Ester 1996; Lapenta et al. 2022). If there is a number of X points (or O points) with a distance of less than $0.5 d_{e0}$ (where d_{e0} is the electron inertial length in the upstream region, $d_{e0} = \sqrt{m_e/m_i} d_{i0}$) from each other, they will be classified into the same X point cluster. Then, each cluster is replaced by a single point located at the average position of the points it contains.

The locations of identified X points and O points at $\Omega_{i0} = 13.01$ are marked in Figure 3(a). Figure 3(b) shows the distributions of the X and O points on the x -axis. The number density of X and O points both peaks near the shock front ($x = 126.5$ – $128 d_{i0}$). Therefore, this region is an active area for the occurrence of magnetic reconnection, which is understandable because the shock front is the location where current sheets generated in the foot region are squeezed and distorted. In the downstream region ($x > 128.5 d_{i0}$), the number densities of X and O points become relatively small. However, no clear decay of these number densities is observed as the plasma convects further downstream of the shock.

For more collective properties of the X points, we have identified all the X points that appeared during the three

reformation cycles shown in Figure 1 ($\Omega_{i0}t = 9$ – 13.61 , with a time interval $\Delta t = 0.02 \Omega_{i0}^{-1}$) and examined them statistically. We define the shock location (x_{sh}) at different times as the position with the largest \bar{B} on the x -axis, then statistical results obtained at all time steps are superposed in the shock rest frame $x' = x - x_{sh}$. To avoid any numerical error caused by sampling on a single mesh grid, physical quantities about reconnection are obtained by averaging at grid points that are less than $0.2 d_{e0}$ away from the X point. Figure 4 shows the statistical properties of the reconnection electric field E_R . Here E_R is the z -component of the nonideal electric field $\mathbf{E}' = \mathbf{E} + \mathbf{V}_e \times \mathbf{B}$ at each X point. In the shock foot region ($x' < -1.0 d_{i0}$), very few X points are detected (Figure 4(b)). However, the reconnection electric field is relatively large and variable, indicating many X points in this region are reconnecting rapidly (Figure 4(a)). Being consistent with Figure 3(b), the count rate of X points also peaks near the shock front (Figure 4(b), $x' = -0.5$ – $0.8 d_{i0}$). The average reconnection electric field remains at about $0.65 V_{A0} B_0$ in this region, which is significantly larger than that in the downstream region (Figure 4(a), $x' > 5 d_{i0}$). This suggests that reconnection in the shock front is not only denser but also more active than that in other regions. Behind the shock front, a clear decay of the reconnection electric field can be observed at $x' = 0.8$ to $5 d_{i0}$, while there is no significant change in the count rates. Note that the X points are just saddle points in magnetic field topology instead of active reconnection sites, and this indicates the reconnection processes decline as they are transported away from the shock by the downward flows. This is because the current sheets experience stronger compression near the shock front; they are thus thinner and reconnect rapidly therein. As they are transferred downstream, they become thick, and the reconnection electric field becomes weak. A quasi-steady state is finally reached in the downstream region ($x > 5 d_{i0}$), where

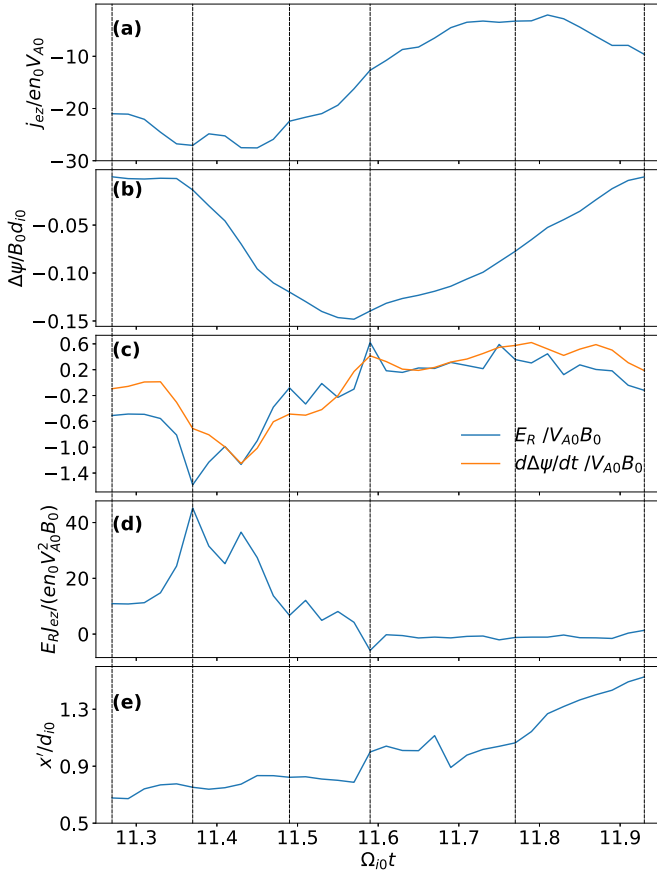


Figure 7. Evolution of different physical values at a traced X point from $\Omega_{i0}t = 11.27$ – 11.93 . (a) Electron current in the z -direction. (b) The magnetic flux between the traced X and O points $\Delta\psi = \psi_X - \psi_O$. (c) Reconnection electric field E_R (blue line) and the gradient of the magnetic flux $\frac{d\Delta\psi}{dt}$ (orange line). (d) The conversion efficiency of electromagnetic energy in z -direction at the X point $E_R j_{ez}$. (e) Distance between the X point and the shock front (x').

both the average reconnection electric field and the count rate remain almost unchanged ($|E_R| \sim 0.25V_{A0}B_0$). The reconnection processes are relatively slow in this region. The total distribution of $|E_R|$ for all the X points is presented in Figure 4(c). While the low reconnection electric field ($|E_R| < 0.25V_{A0}B_0$) exhibits a Maxwell distribution, there is a power-law distribution toward higher $|E_R|$.

The distributions of the reconnection electric field and the guide field B_g are presented in Figure 5. Here the guide field B_g is the out-of-plane (z) component of the magnetic field at each X point. Most of the X points have a reconnection electric field of about $0.25V_{A0}B_0$ and a guide field of 2.2 to $3.7B_0$, which is larger than the background guide field we set up at the beginning ($B_{0z} = 0.966B_0$). For those X points with larger reconnection electric field ($|E_R| > 0.55V_{A0}B_0$), there is a correlation between these two values. These X points are active reconnection sites mainly located near the shock front, and their reconnection electric field grows as the guide field increases. This is because that strong compression causes both a large guide field and a large reconnection electric field.

3.2. Evolution of Reconnection Events

Statistics in Section 3.1 show a general distribution of the reconnection electric field (E_R) at different locations. However, it remains unclear how a single reconnection event evolves

temporally and whether E_R can be used as a standard measure to quantify the intensity of reconnection in a turbulent environment. In this section, we trace two representative X points located near the shock front and in the downstream region respectively, and explore the evolution of reconnection at these points.

The first X point we trace is generated at $x = 133.2d_{i0}$, $y = 3.8d_{i0}$ at $\Omega_{i0}t = 11.27$. To determine whether reconnection at the X point is ongoing at different times, we examine the divergence of magnetic flux transport $\nabla \cdot \mathbf{U}_\psi$, where \mathbf{U}_ψ is the in-plane magnetic flux transport velocity given by $\mathbf{U}_\psi = \frac{cE_z(\mathbf{e}_z \times \mathbf{e}_{B_p})}{B_p}$ and \mathbf{e}_{B_p} is the unit vector of the in-plane magnetic field \mathbf{B}_p (Li et al. 2021). The direction of \mathbf{U}_ψ is perpendicular to the in-plane magnetic field and always exhibits a converging inflow and diverging outflow near the X point. Then, $\nabla \cdot \mathbf{U}_\psi$ can consistently show a quadrupolar structure at all reconnection sites in turbulence as $\nabla \cdot \mathbf{U}_\psi < 0$ and > 0 capture the inflows and outflows of magnetic flux, respectively. Figure 6 shows $\nabla \cdot \mathbf{U}_\psi$ at the X point at six different times. In addition, we also show in Figure 7 the out-of-plane electron current J_{ez} , the reconnection electric field E_R , the magnetic flux between the X point and the O point $\psi_X - \psi_O$, the conversion rate of electromagnetic energy in z -direction $E_R J_{ez}$, and the position relative to the shock front x' .

At the beginning ($\Omega_{i0}t = 11.27$; see Figure 6(a)), reconnection is triggered in an electron-scale current sheet near the shock front ($x' \sim 0.65d_{i0}$). The reconnection electric field E_R increases from $-0.54V_{A0}B_0$ to $-1.6V_{A0}B_0$ at $\Omega_{i0}t = 11.37$ (see Figure 7(c)). During this time, the magnetic flux between the X point and the O point increases rapidly, leading to the formation of the magnetic island located at $x' \sim 0.725d_{i0}$, $y \sim 3.834d_{i0}$ (Figure 6(b)). According to the clear quadrupolar structure in Figures 6(a) and 6(b), magnetic flux flows in from the x -direction and flows out in the y -direction approximately. This rapid reconnection state does not last for a long time; as the X point is being transported away from the shock front, E_R drops to $-0.1V_{A0}B_0$ at $\Omega_{i0}t = 11.49$ (Figure 7(c)) and the inflow of magnetic flux becomes unclear (Figure 6(c)). After $\Omega_{i0}t = 11.49$, E_R remains relatively small (Figure 7(c)), and the magnetic flux changes slowly (Figure 7(b)). The shock transition region is filled with turbulent flows, which can possibly affect the state of reconnection by converging or diverging from each other. This process is observed at $\Omega_{i0}t = 11.59$, when E_R changes its sign abruptly and becomes about $0.57V_{A0}B_0$ (Figure 7(c)). The inflow direction of reconnection becomes the outflow direction and vice versa, which can be seen in Figures 6(d) and (e). During this time, the magnetic island we traced merges with the magnetic island below, and its magnetic flux declines (Figure 7(b); $\Omega_{i0}t = 11.59$ – 11.93). Finally, at $\Omega_{i0}t = 11.93$, the X and O points we trace vanish, and the reconnection stops (Figure 6(f)). During the entire time period, the reconnection electric field E_R matches the change of magnetic flux between the X and O points. Namely, the magnetic flux changes rapidly when E_R is large, and the magnetic flux decreases when E_R becomes negative. This confirms that E_R can be used as a standard measure to quantify the intensity of reconnection in turbulent environments, making the statistics in Section 3.1 more convincing. The reconnection electric field can efficiently accelerate particles in the z -direction when the X point is near the shock front (Figure 7(d); $\Omega_{i0}t = 11.27$ – 11.49), while the

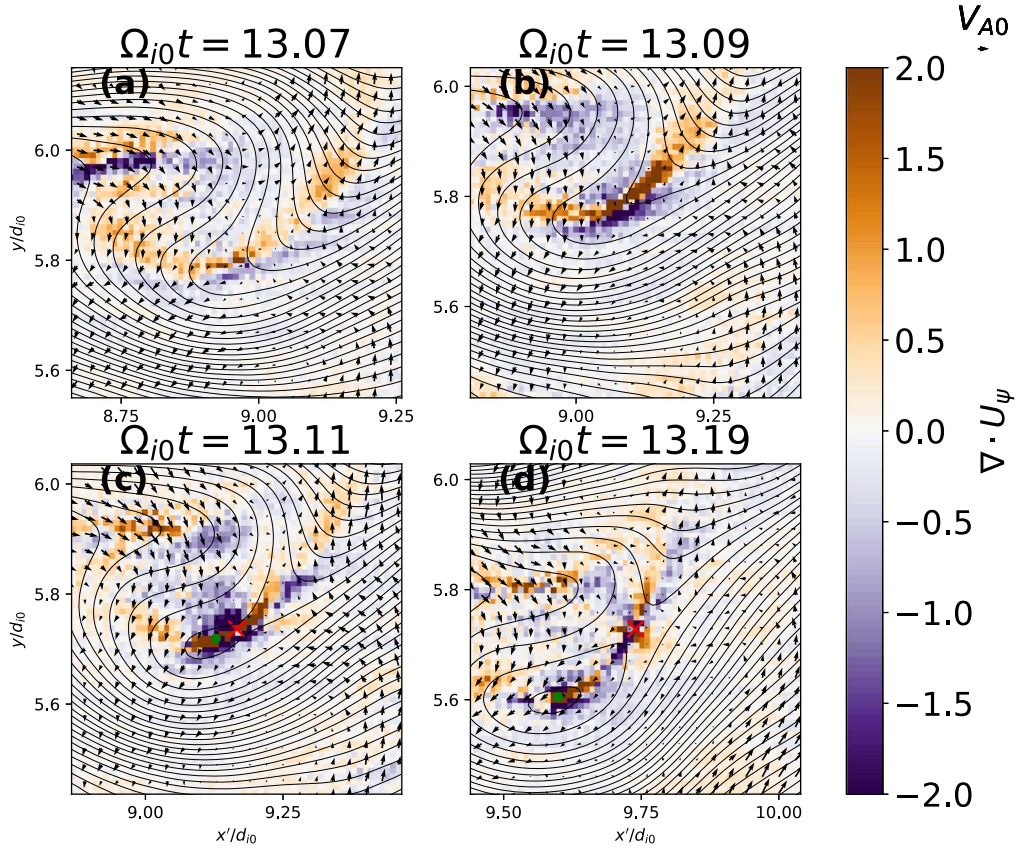


Figure 8. Divergence of the magnetic flux transport $\nabla \cdot \mathbf{U}_\psi$ at a traced X point at $\Omega_{i0}t = 13.07, 13.09, 13.11,$ and 13.19 . The black lines represent the in-plane magnetic field line. Black arrows are the in-plane electron velocity minus the mean flow in the drawn area. The X and O points we traced are marked by the red “X” and green dot. An animation of this figure shows the evolution of the current sheet from $\Omega_{i0}t = 12.99$ to 13.37 .

(An animation of this figure is available.)

energy conversion becomes weak and even negative when E_R is relatively small (Figure 7(d); $\Omega_{i0}t = 11.49$ – 11.93).

Although the X and O points formed near the shock front may vanish when they are convected away from the shock just like in Figure 6, no clear decay of their number density is found in the downstream region (Figures 3(b) and 4(b)). This indicates a portion of these X and O points are generated by the downstream turbulent flow locally in addition to being originated from the shock front. In Figure 8, we show the formation of a new X point in the downstream region. At $\Omega_{i0}t = 13.07$, a current sheet located at about $x' = 9.0d_{i0}$, $y = 5.8d_{i0}$ is stretched by the electron flow: Electrons in $x' > 9.0d_{i0}$ and $y > 5.8d_{i0}$ flow to the upper right, while electrons in $x' < 9.0d_{i0}$ and $y < 5.8d_{i0}$ flow to the lower left (Figure 8(a)). A magnetic cavity is then generated around $x' = 9.05d_{i0}$, $y = 5.76d_{i0}$ at $\Omega_{i0}t = 13.09$, and a quadrupolar structure of $\nabla \cdot \mathbf{U}_\psi$ starts to be detected (Figure 8(b)). As the electron flow further stretches the current sheet, an X point and an O point is formed at $\Omega_{i0}t = 13.11$ (Figure 8(c)). Reconnection at the X point undergoes rapidly, forming a magnetic island at $\Omega_{i0}t = 13.19$ (Figure 8(d)). This kind of reconnection, which is driven by the turbulent flow, can occur over a wide range downstream of the shock and even in the magnetosheath.

4. Conclusions and Discussion

In this paper, we have performed a 2D PIC simulation of a quasi-perpendicular collisionless shock. The angle between the upstream magnetic field and shock normal (θ_{Bn}) is 75° , and the

Alfvén Mach number is about 10, which are typical parameters for Earth’s bow shock and interplanetary shocks in the solar wind (Balogh & Treumann 2013). An electron-scale current sheet is formed in the foot region during the shock reformation, which is then distorted and fragmented as it is convected to the shock front by the solar wind. Magnetic reconnection can thus occur in the turbulent shock transition and downstream region, producing multiple magnetic islands. This mechanism can take place in a moderate-Mach-number shock such as Earth’s bow shock, which is different from the reconnection at the fragmented shock foot caused by ion Weibel instability in high-Mach-number perpendicular shocks (Matsumoto et al. 2015).

By employing a saddle-point identification method, we have picked out all the points at which the topology of the magnetic field lines changed (X and O points). The number of these X and O points peaks at the shock front and is less in the downstream region. Observation in the shock transition region made by MMS has suggested that the population of reconnection events is well localized to the shock ramp (Gingell et al. 2020), which is consistent with our results. Nevertheless, we point out that the number does not keep decreasing as one goes further downstream for at least $10d_{i0}$. Our tracing of individual X points further indicates that, although reconnection sites formed near the shock front may vanish during their transport away from the shock, new X points can be generated by the turbulent flow locally in the downstream region, making the number density of X points

almost unchanged. Near the shock front, the compression is much larger than in the downstream region, making the current sheets also thinner. As a result, magnetic reconnection has a larger reconnection electric field and proceeds faster than in the downstream region. In other words, the shock front is not only a region containing dense reconnection sites but also a position where reconnection undergoes actively.

It should be noted that our simulation adopts an out-of-plane configuration, where the magnetic field has a prominent component perpendicular to the simulation plane. Compared to the in-plane configuration (Gingell et al. 2023), the chosen plane in our study is conducive to magnetic reconnection due to the ease with which even small perturbations can generate current sheets with alternating magnetic polarities. Consequently, most reconnection events in our simulation exhibit a strong guide field, while a range of guide fields and current sheet orientations have been observed in three-dimensional quasi-parallel shock simulations (Ng et al. 2022). Considering this, it would be worthwhile to explore reconnection statistically at quasi-perpendicular shocks using a three-dimensional PIC model in future studies. In addition, the importance of magnetic reconnection described in this paper to the overall energy conversion associated with the shock is still unknown. Further investigation is necessary to fully understand its energy contribution.

Acknowledgments

This work was supported by the NSFC grant No. 42174181 and the Strategic Priority Research Program of Chinese Academy of Sciences grant No. XDB41000000. Computation resources were provided by the Hefei Advanced Computing Center of China.

ORCID iDs

Ao Guo  <https://orcid.org/0000-0002-7625-7625>

Quanming Lu  <https://orcid.org/0000-0003-3041-2682>

San Lu  <https://orcid.org/0000-0003-2248-5072>

Shimou Wang  <https://orcid.org/0000-0002-4382-1349>

Rongsheng Wang  <https://orcid.org/0000-0002-9511-7660>

References

Bale, S. D., Balikhin, M. A., Horbury, T. S., et al. 2005, *SSRv*, **118**, 161
 Balogh, A., & Treumann, R. A. 2013, *Physics of Collisionless Shocks: Space Plasma Shock Waves* (New York: Springer)
 Bavassano-Cattaneo, M. B., Tsurutani, B. T., Smith, E. J., et al. 1986, *JGR*, **91**, 11929
 Bessho, N., Chen, L.-J., Wang, S., et al. 2019, *GeoRL*, **46**, 9352
 Bessho, N., Chen, L.-J., Wang, S., et al. 2020, *PhPI*, **27**, 092901
 Bessho, N., Chen, L.-J., Stawarz, J. E., et al. 2022, *PhPI*, **29**, 042304

Biskamp, D., & Welter, H. 1972, *PhRvL*, **28**, 410
 Burgess, D., Lucek, E. A., Scholer, M., et al. 2005, *SSRv*, **118**, 205
 Burgess, D., & Scholer, M. 2007, *PhPI*, **14**, 012108
 Comisso, L., & Sironi, L. 2018, *PhRvL*, **121**, 255101
 Comisso, L., & Sironi, L. 2022, *ApJL*, **936**, L27
 Derouillat, J., Beck, A., Pérez, F., et al. 2018, *CoPhC*, **222**, 351
 Dimmock, A. P., Russell, C. T., Sagdeev, R. Z., et al. 2019, *SciA*, **5**, eaau926
 Ester, M., Kriegl, H.-P., Sander, J., & Xu, X. 1996, in Proc. Second Int. Conf. on Knowledge Discovery and Data Mining (KDD'96), ed. E. Simoudis, J. Han, & U. Fayyad (Washington, DC: AAAI Press), 226
 Gingell, I., Schwartz, S. J., Eastwood, J. P., et al. 2019, *GeoRL*, **46**, 1177
 Gingell, I., Schwartz, S. J., Eastwood, J. P., et al. 2020, *JGRA*, **125**, e27119
 Gingell, I., Schwartz, S. J., Kucharek, H., et al. 2023, *PhPI*, **30**, 012902
 Gumett, D. A., Neubauer, F. M., & Schwenn, R. 1979, *JGR*, **84**, 541
 Haggerty, C. C., Parashar, T. N., Matthaeus, W. H., et al. 2017, *PhPI*, **24**, 102308
 Hao, Y., Lu, Q., Gao, X., et al. 2014, *JGRA*, **119**, 3225
 Hao, Y., Lu, Q., Gao, X., et al. 2016, *ApJ*, **823**, 7
 Lapenta, G., Goldman, M., Newman, D. L., et al. 2022, *ApJ*, **940**, 187
 Lazarian, A., & Vishniac, E. T. 1999, *ApJ*, **517**, 700
 Lazarian, A., Eyink, G. L., Jafari, A., et al. 2020, *PhPI*, **27**, 012305
 Le, G., & Russell, C. T. 1992, *P&SS*, **40**, 1203
 Lembège, B., & Dawson, J. M. 1987, *PhPI*, **30**, 1767
 Lembège, B., & Savoini, P. 2002, *JGRA*, **107**, 1037
 Li, T. C., Liu, Y.-H., & Qi, Y. 2021, *ApJL*, **909**, L28
 Li, X., Wang, R., Lu, Q., et al. 2022, *NatCo*, **13**, 3241
 Lobzin, V. V., Krasnoselskikh, V. V., Bosqued, J.-M., et al. 2007, *GeoRL*, **34**, L05107
 Lu, Q., & Wang, S. 2005, *GeoRL*, **32**, L03111
 Lu, Q., Wang, H., Wang, X., et al. 2020a, *GeoRL*, **47**, e85661
 Lu, Q., Yang, Z., Wang, H., et al. 2021, *ApJ*, **919**, 28
 Lu, S., Lu, Q., Wang, R., et al. 2022, *GeoRL*, **49**, e98547
 Lu, S., Wang, R., Lu, Q., et al. 2020b, *NatCo*, **11**, 5049
 Matsukiyo, S., & Scholer, M. 2003, *JGRA*, **108**, 1459
 Matsukiyo, S., & Scholer, M. 2006, *JGRA*, **111**, A06104
 Matsumoto, Y., Amano, T., Kato, T. N., et al. 2015, *Sci*, **347**, 974
 McKean, M. E., Winske, D., & Gary, S. P. 1992, *JGR*, **97**, 19421
 Ng, J., Chen, L.-J., Bessho, N., et al. 2022, *GeoRL*, **49**, e99544
 Phan, T. D., Eastwood, J. P., Shay, M. A., et al. 2018, *Natur*, **557**, 202
 Pyakurel, P. S., Shay, M. A., Phan, T. D., et al. 2019, *PhPI*, **26**, 082307
 Retinò, A., Sundkvist, D., Vaivads, A., et al. 2007, *NatPh*, **3**, 236
 Russell, C. T., Hoppe, M. M., & Livesey, W. A. 1982, *Natur*, **296**, 45
 Sagdeev, R. Z. 1966, *RvPP*, **4**, 23
 Scholer, M. 1990, *GeoRL*, **17**, 1821
 Servidio, S., Matthaeus, W., Shay, M., et al. 2009, *PhRvL*, **102**, 115003
 Servidio, S., Matthaeus, W. H., Shay, M. A., et al. 2010, *PhPI*, **17**, 032315
 Stawarz, J. E., Eastwood, J. P., Phan, T. D., et al. 2019, *ApJL*, **877**, L37
 Su, Y., Lu, Q., Huang, C., et al. 2012, *JGRA*, **117**, A08107
 Tsurutani, B. T., & Stone, R. G. 1985, *Geophysical Monograph*, Vol 34 (Washington, DC: American Geophysical Union),
 Turner, D. L., Wilson, L. B., Liu, T. Z., et al. 2018, *Natur*, **561**, 206
 Vörös, Z., Yordanova, E., Varsani, A., et al. 2017, *JGRA*, **122**, 11442
 Wang, R., Lu, Q., Nakamura, R., et al. 2018, *GeoRL*, **45**, 4542
 Wang, S., Chen, L.-J., Bessho, N., et al. 2019, *GeoRL*, **46**, 562
 Wang, S., Wang, R., Lu, Q., et al. 2021, *GeoRL*, **48**, e94879
 Wu, M., Hao, Y., Lu, Q., et al. 2015, *ApJ*, **808**, 2
 Yang, Z. W., Liu, Y. D., Johlander, A., et al. 2020, *ApJL*, **901**, L6
 Yang, Z. W., Lu, Q. M., Lembege, B., & Wang, S. 2009, *JGRA*, **114**, A03111
 Yordanova, E., Vörös, Z., Varsani, A., et al. 2016, *GeoRL*, **43**, 5969
 Zhong, Z. H., Zhou, M., Liu, Y.-H., et al. 2022, *ApJL*, **926**, L27